J Adv Ceram

Research Article

Enhancing microwave dielectric properties of Li_2TiO_3 ceramics via monoclinic–cubic phase transition control

Zuwei Wang[1,2,3,4,†], Huanhuan Guo[1,2,3,4,†,✉], Yueming Li[1,2,3,✉], Yuanyuan Huang[1], Yuhui Wang[1], Zong-Yang Shen[1,2,3]

Cite this article: Wang Z, Guo H, Li Y, et al. *J Adv Ceram* 2026, **15**(6): 9221305. https://doi.org/10.26599/JAC.2026.9221305

ABSTRACT: Lightweight β-Li_2TiO_3 ceramics are promising microwave dielectrics for the large-scale deployment of 5.5G extremely large antenna arrays (ELAAs). However, their practical application is hindered by the limited $Q\times f$ value (where quality factor Q = 1/dielectric loss (tanδ), and f represents the resonant frequency) and large positive temperature coefficient of resonant frequency (TCF), while the underlying phase transition and regulatory mechanisms remain elusive. Here, a unique monoclinic–cubic dual-phase architecture is constructed in $Li_2Ti_{1-x}(Sc_{1/2}Nb_{1/2})_xO_3$ (LTSN$_x$, $0 \le x \le 0.5$) ceramics. *In situ* structural characterizations reveal that the substitution-induced reduction in the phase transition temperature (T_c) and concomitant lattice distortion synergistically impede the reversed-phase transformation, stabilizing the high-temperature cubic phase at room temperature. Consequently, the inherent negative TCF of the cubic phase effectively compensates for the positive value of the monoclinic matrix, achieving exceptional temperature stability. Furthermore, the reconstructed superlattices and suppression of lattice defects significantly minimize dielectric loss. Of particular importance is that the studied $LTSN_{0.25}$ ceramic exhibits excellent microwave dielectric properties, featuring a relative permittivity (ε_r) of 18.6, ultra-high $Q\times f$ of 102,330 GHz (at 7.76 GHz), and a near-zero TCF of −2.3 ppm/°C. Simultaneously, the stable THz response and simulated filter performance confirm its great potential for 5.5G applications.

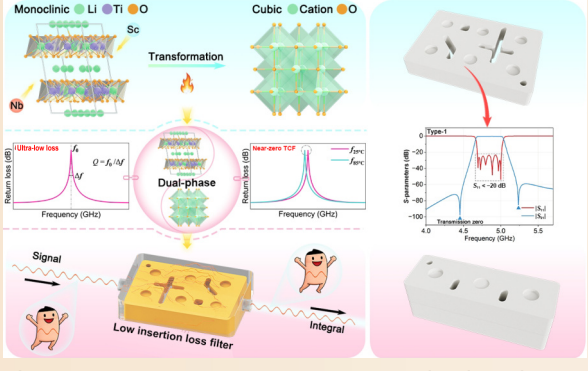

KEYWORDS: 5.5G; microwave dielectric ceramics; ultra-low loss; near-zero temperature coefficient of resonant frequency (TCF); filter

1 Introduction

With the global rollout of 5.5G (5G-Advanced), the performance frontiers of communication networks are being propelled to unprecedented heights of 10 Gbps downlink and 1 Gbps uplink, imposing stringent requirements on the radio frequency (RF) capabilities and deployment density of base stations [1,2]. Owing to their high gain and massive capacity, extremely large antenna arrays (ELAAs) have emerged as the cornerstone of 5.5G infrastructure, thereby triggering an urgent demand for next-generation advanced dielectric filters and antennas [3–5]. As the foundational material for RF devices, microwave dielectric ceramics are required to simultaneously exhibit superior intrinsic properties—specifically, a suitable dielectric constant (ε_r), ultra-low loss (high quality factor Q), and near-zero temperature coefficient of resonant frequency (TCF). To accommodate the massive scale of 5.5G deployment, these materials must simultaneously fulfill industrial prerequisites for cost-effective manufacturing and lightweight design [6–8]. However, achieving an optimal balance among these rigorous multidimensional criteria remains a formidable challenge.

Monoclinic lithium titanate (β-Li_2TiO_3, LTO) has garnered significant attention across diverse fields, ranging from nuclear fusion and lithium-ion batteries to microwave dielectric ceramics, owing to its exceptional physicochemical stability and structural versatility [9–11]. Moreover, its facile synthesis and abundant precursors ensure the economic viability essential for mass manufacturing. However, the intrinsic microwave dielectric

† Zuwei Wang and Huanhuan Guo contributed equally to this work.

[1] School of Materials Science and Engineering, Jingdezhen Ceramic University, Jingdezhen 333403, China. [2] Jiangxi Key Laboratory of Advanced Ceramic Materials, Jingdezhen Ceramic University, Jingdezhen 333403, China. [3] China National Light Industry Key Laboratory of Functional Ceramic Materials, Jingdezhen 333403, China. [4] National Engineering Research Center for Domestic & Building Ceramics, Jingdezhen Ceramic University, Jingdezhen 333403, China.

✉ Corresponding authors. E-mail: H. Guo, guohuanhuan@jcu.edu.cn; Y. Li, lym6329@163.com

Received: February 24, 2026; Revised: April 9, 2026; Accepted: April 25, 2026

properties of LTO remain suboptimal, falling short of the exacting requirements for high-performance microwave devices. Specifically, its relatively low $Q\times f$ value (~23,600 GHz, where Q = 1/dielectric loss (tanδ), and f represents the resonant frequency) leads to exacerbated insertion loss, significantly compromising the overall energy efficiency and signal integrity [12]. Compounding this issue, its large positive TCF (~+38.5 ppm/°C) undermines frequency stability over wide operating temperature ranges [13]. Particularly for base stations deployed in high-latitude or high-altitude regions characterized by severe thermal fluctuations, such thermal instability is unacceptable. To surmount these performance bottlenecks, contemporary research efforts have primarily centered on modification strategies such as ceramic composites and ionic substitution [14–16]. For instance, Zuo *et al.* [17] successfully tuned the TCF to ~−7.4 ppm/°C ($\varepsilon_r \approx 21.2$, $Q\times f \approx$ 59,039 GHz) by constructing $0.86Li_2TiO_3$–$0.14Li_2CeO_3$ composite ceramics, strategically exploiting the compensation effect between components with opposing thermal coefficients. Nevertheless, this strategy entails addressing complex challenges related to sintering temperature mismatch, chemical stability, and interfacial effects. Furthermore, the introduction of heterogeneous phases inevitably induces extrinsic defects or impurities, usually degrading the $Q\times f$ value. For example, the Li_2TiO_3–30 vol% $Li_2Zn_3Ti_4O_{12}$ system, while achieving a near-zero TCF (~−1.3 ppm/°C), exhibits ε_r of 22.0 and limited $Q\times f$ of 38,900 GHz [18]. Additionally, the temperature dependence of TCF prevalent in simple composites can mask actual frequency drift, potentially misleading practical applications [19,20].

In contrast, the strategy of inducing phase evolution via ionic substitution, exemplified by the ferroelastic phase transitions in $BiVO_4$ and $SmNbO_4$ systems, is regarded as a superior and more efficient approach for comprehensively regulating microwave dielectric properties [21–24]. Investigations have revealed that monoclinic rock-salt LTO undergoes a transformation to a cubic rock-salt phase at elevated temperatures, accompanied by a cation order–disorder transition [25,26]. Simultaneously, rock-salt structured compounds typically exhibit extensive solid solubility ($0.42 \le R_A/R_X \le 0.72$, where R_A and R_X denote the cation and anion radii, respectively), providing broad latitude for ionic substitution design [27]. Notably, continuous phase transitions induced by ionic substitution have been observed in LTO-based systems, such as $Li_2Ti_{1-x}(Cu_{1/3}Nb_{2/3})_xO_3$, $Li_2Ti_{1-x}(Zn_{1/3}Ta_{2/3})_xO_3$, and $Li_2Ti_{1-x}(Mg_{1/3}Nb_{2/3})_xO_3$, accompanied by enhanced microwave dielectric properties [28–30]. Despite the proven efficacy of ionic substitution, a systematic and in-depth understanding of how substitution precisely drives phase transitions, as well as the intrinsic structure–property relationship between phase evolution and microwave performance, remains elusive. Therefore, unraveling these intrinsic correlations and underlying mechanisms is pivotal for guiding the rational design of high-performance LTO-based microwave dielectric ceramics.

Herein, novel $Li_2Ti_{1-x}(Sc_{1/2}Nb_{1/2})_xO_3$ (LTSN$_x$) microwave dielectric ceramics were designed and synthesized via a $(Sc_{1/2}Nb_{1/2})^{4+}$ complex ion substitution strategy targeting the Ti^{4+} site. Firstly, Sc^{3+} exhibits a unique electronic configuration characterized by empty 3d orbitals ([Ar]4s^{0}3d^0), which is distinguished from conventional lanthanide rare-earth elements (such as Nd^{3+}, Sm^{3+}, and Ce^{3+}) that possess partially filled 4f orbitals [31,32]. This specific configuration fundamentally eliminates dielectric loss arising from d–d electron transitions [33]. Concurrently, Nb^{5+} ([Kr]5s^{0}4d^0), sharing the same d^0 electronic configuration, was incorporated to maintain charge balance and suppress lattice defects, thereby further unlocking the ultra-high Q potential of LTO (as illustrated in Fig. S1 in the Electronic Supplementary Material (ESM)) [34,35]. Secondly, the $(Sc_{1/2}Nb_{1/2})^{4+}$ complex ion possesses an electronegativity comparable to that of Ti^{4+} (1.48 vs. 1.54), favoring the substitution process. Meanwhile, the appropriate ionic radius mismatch (0.693 vs. 0.605 Å, $\Delta R/R$ = 14.5%) is sufficient to introduce local lattice strain, thereby inducing the desired phase transition. Guided by this design rationale, this study systematically investigates the influence of ion substitution on LTO lattice evolution, aiming to establish an intrinsic structure–property relationship between crystal structure and microwave dielectric performance. Furthermore, a dielectric waveguide filter was designed using the optimal LTSN$_{0.25}$ ceramic to demonstrate its potential for sub-6 GHz applications.

2 Experimental

2.1 Sample synthesis

LTSN$_x$ ($0 \le x \le 0.5$) ceramics were synthesized via a conventional solid-state reaction method using high-purity Li_2CO_3 (99.99%), Nb_2O_5 (99.5%), Sc_2O_3 (99.99%), and TiO_2 (99.9%) powders. First, the raw materials were weighed according to the stoichiometric formulations and ball-milled for 4 h in anhydrous ethanol using zirconia balls as the milling media. The resulting slurries were dried at 80 °C for 12 h, followed by calcination at 1000 °C for 2 h to form the main crystalline phase. The calcined powders were re-milled for 4 h, dried, and granulated with a 5 wt% polyvinyl alcohol (PVA) binder solution. Subsequently, the powders were uniaxially pressed into cylindrical samples (10 mm in diameter and 4–5 mm in height). These samples were initially heated at 550 °C for 4 h to remove the organic binder and finally sintered at 1175–1250 °C for 2 h to obtain the dense ceramics.

2.2 Material characterizations

The phase composition of the sintered ceramics was identified by X-ray diffraction (XRD; D8-Advance, Bruker, Germany). Rietveld refinement was performed on the XRD data using the GSAS-II software to obtain the phase weight fractions. *In situ* high-temperature XRD (HT-XRD) patterns were collected using an X-ray diffractometer (XRDynamic 500, Anton Paar, Austria). Room-temperature and temperature-dependent Raman spectra were acquired over a wavenumber range of 100–1000 cm^{-1} with a Raman spectrometer (inVia, Renishaw, UK) equipped with a 532 nm excitation laser operating at a low power (10 mW). The bulk densities of the sintered ceramics were measured by the Archimedes method using deionized water as the liquid medium. The phase distribution and crystal orientation were analyzed via electron backscatter diffraction (EBSD; Symmetry 2, Oxford Instruments, UK). The microstructural morphology was characterized by field-emission scanning electron microscopy (FESEM; Sigma 300, ZEISS, Germany), and the average grain sizes were evaluated using the linear intercept method via ImageJ software. High-resolution transmission electron microscopy (HRTEM) images and selected area electron diffraction (SAED) patterns were obtained using a field-emission transmission electron microscope (STEM; JEM-F200, JEOL, Japan). The surface elemental composition and chemical states were analyzed by X-ray photoelectron spectroscopy (XPS; Nexsa, Thermo Fisher Scientific, USA), and the data were processed using Avantage software. The coefficient of thermal expansion (CTE) was measured using a dilatometer (DIL 402 C, NETZSCH, Germany) in the temperature range of 25–1300 °C. Optical absorption spectra were recorded using an ultraviolet–visible (UV–Vis)

spectrophotometer (Lambda 850, PerkinElmer, USA). Finally, microwave dielectric properties were evaluated using a network analyzer (HP8720B, Agilent, USA) equipped with a temperature chamber based on the transverse electric 01δ mode ($TE_{01\delta}$) dielectric resonator method. The TCF value was measured in the temperature range of 25–85 °C and calculated using Eq. (1):

$$\mathrm{TCF} = \frac{f_{85} - f_{25}}{(85 - 25) \times f_{25}} \times 10^6 \quad (1)$$

where f_{85} and f_{25} are the $TE_{01\delta}$ resonant frequencies at temperatures of 85 and 25 °C, respectively. Furthermore, the terahertz (THz) spectra were recorded using a terahertz time-domain spectroscopy system (TAS7400TS, Advantest, Japan). The 3D electromagnetic simulations for the filter design were performed using CST STUDIO software. The infrared thermal images were captured utilizing an infrared thermal imaging camera (Fluke Ti480U, Fluke, USA) to evaluate the thermal distribution.

3 Results and discussion

Figure 1(a) presents the powder X-ray diffraction (PXRD) patterns of $LTSN_x$ ($0 \le x \le 0.5$) ceramics obtained at optimum sintering temperatures. No impurity phases were observed in any composition, confirming high phase purity. Pure monoclinic LTO features a rock-salt superstructure along the [001] direction, characterized by the periodic alternating arrangement of Li layers and mixed $[Li_{1/3}Ti_{2/3}]$ layers [26,36]. Consequently, a prominent (002) diffraction peak is observed in the low Bragg angle region ($2\theta \approx 18°$) [37]. With the progressive substitution of $(Sc_{1/2}Nb_{1/2})^{4+}$ for Ti^{4+}, a continuous monoclinic-to-cubic phase transition is induced within the range of $0.1 \le x \le 0.5$, as clearly evidenced by the evolution of diffraction peak intensities. Specifically, within the range of $0.1 \le x \le 0.3$, the system forms a monoclinic–cubic dual-phase solid solution. Arising from an *in situ* phase transition, this dual-phase structure exhibits unique polymorphic characteristics. During this transition, the relative intensity of the monoclinic (002) superstructure peak gradually diminishes, while the cubic

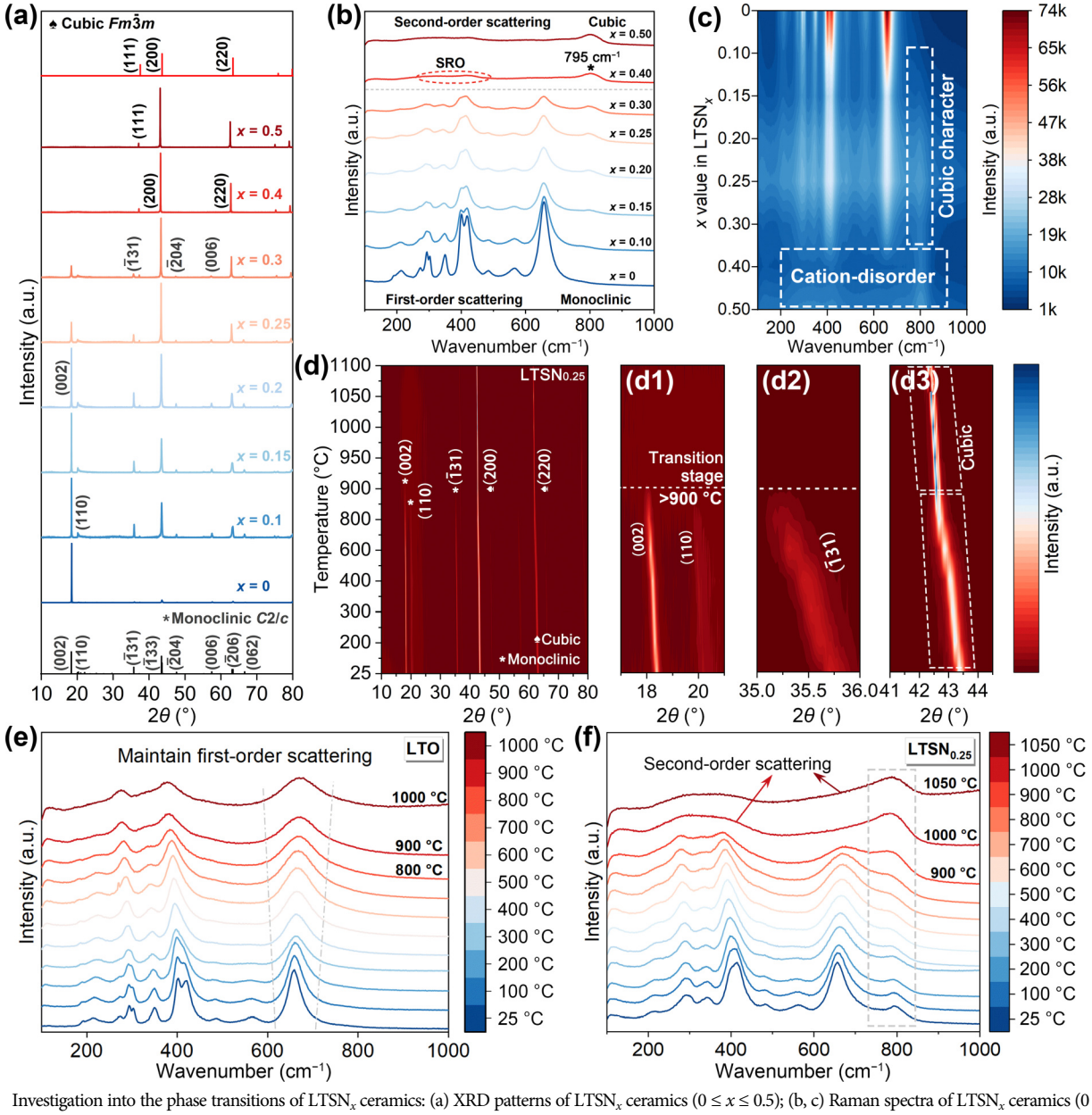

Fig. 1 Investigation into the phase transitions of $LTSN_x$ ceramics: (a) XRD patterns of $LTSN_x$ ceramics ($0 \le x \le 0.5$); (b, c) Raman spectra of $LTSN_x$ ceramics ($0 \le x \le 0.5$); (d) *in situ* high-temperature XRD patterns of $LTSN_{0.25}$ ceramic; *in situ* high-temperature Raman spectra of (e) LTO and (f) $LTSN_{0.25}$ ceramics, respectively.

(200) and (220) peaks concurrently intensify with increasing x. At $x \geq 0.4$, the complete extinction of the (002) peak and other characteristic monoclinic reflections signify a full transformation to the disordered cubic ($Fm\bar{3}m$) structure. To quantitatively elucidate this process, Rietveld refinements were performed on the XRD patterns. The detailed refined profiles are presented in Figs. S2(a)–S2(g) in the ESM. The quantitative results (Fig. S2(h) in the ESM) reveal a monotonic variation in phase fractions, explicitly confirming the continuous nature of the phase transition.

Raman spectroscopy, owing to its high sensitivity to local symmetry variations and cationic arrangements, is widely employed to characterize structural evolution. As depicted in Fig. 1(b), all $LTSN_x$ samples within the range of $0.1 \leq x \leq 0.3$ exhibit vibration modes analogous to those of pure monoclinic LTO. Based on group theory analysis, for the monoclinic structure belonging to the $C2/c$ space group (point group C_{2h}), the Raman-active vibrational modes are described by the irreducible representation: $\Gamma_{Raman} = 15A_g + 18B_g$ [38]. Consistent with this prediction, the spectra exhibit numerous sharp vibrational modes, which are characteristic of the cation-ordered monoclinic structure. To identify specific vibrational modes, Fig. S3(a) in the ESM presents the Lorentzian deconvolution results for LTO. The Raman bands in the 210–500 cm^{-1} range are assigned to Li–O stretching and O–Li–O bending vibrations within $[LiO_6]$ octahedra, while those in the 500–700 cm^{-1} region originate from Ti–O stretching vibrations within $[TiO_6]$ octahedra [28,30]. Notably, the intensity of the sharp Raman peaks exhibits a systematic attenuation with increasing substitution (Fig. 1(c)). According to the literature, the Raman scattering intensity is directly proportional to the number of unit cells contributing to specific vibrational modes [39,40]. Therefore, this attenuation is primarily attributed to the decreased volume fraction of the Raman-active monoclinic phase. Concurrently, a significant broadening of the full width at half maximum (FWHM) is observed for the characteristic peaks, as exemplified by the mode at 657 cm^{-1} (Fig. S3(b) in the ESM). This broadening provides clear evidence that $(Sc_{1/2}Nb_{1/2})^{4+}$ substitution leads to the disordering of the local cationic arrangement. At $x \geq 0.4$, the distinct Raman peaks originating from the monoclinic phase disappear completely and are replaced by several broad and weak bands. This spectral feature reflects the complete transformation of $LTSN_x$ ceramics into a long-range disordered cubic phase, aligning perfectly with the XRD results. Crucially, the ideal cubic $Fm\bar{3}m$ structure (point group O_h) possesses a center of inversion symmetry. Consequently, the first-order Raman scattering is theoretically disallowed, resulting in the absence of the first-order Raman activity [41,42]. However, the broad and weak bands observed in the spectra primarily originate from the second-order Raman scattering, described by the irreducible representation: $\Gamma_{Raman} = A_{1g} + E_g + T_{2g}$ [37].

While static correlations between the composition (x) and phase structure are established, the dynamic evolution of the phase structure with temperature remains a critical issue requiring in-depth investigation, especially regarding the formation and retention mechanisms of the high-temperature cubic phase. To this end, *in situ* HT-XRD and Raman spectroscopy (HT–Raman) were employed to characterize the representative $LTSN_{0.25}$ sample. As illustrated in Fig. 1(d) and Fig. S4 in the ESM, the HT–XRD patterns remain stable from 25 to 800 °C, exhibiting only thermal expansion-induced shifts [43]. However, above 900 °C, the monoclinic (002) peak and other characteristic reflections (such as (110), $(\bar{1}31)$, $(\bar{2}06)$, and (062)) rapidly attenuate and nearly vanish. This confirms that the monoclinic phase becomes thermodynamically unstable, driving a complete transformation to the energetically favorable cubic phase above 900 °C. Compared to the reported monoclinic-to-cubic phase transition temperature (T_c) of LTO (~1200 °C), the substitution of $(Sc_{1/2}Nb_{1/2})^{4+}$ significantly lowers T_c to approximately 900 °C [25,43]. This reduction is likely attributed to the lattice strain induced by the ionic radius mismatch, which increases the internal energy and accelerates thermal destabilization [44]. Crucially, this lowered T_c enables direct observation of the phase transition process using conventional *in situ* techniques.

This conclusion is further corroborated by HT–Raman analysis (Fig. 1(f)). Despite the expected thermal broadening and attenuation of Raman peaks from 25 to 800 °C, the characteristic monoclinic modes are well-preserved. Upon further heating (> 900 °C), these characteristic features vanish completely, evolving into broad bands highly consistent with those of the room-temperature cubic phase, such as $LTSN_{0.4}$ (Fig. 1(b)). In sharp contrast, the HT–Raman spectra of LTO (Fig. 1(e)) reveal that its characteristic monoclinic modes persist even up to the testing limit (constrained by Li volatility), confirming that its T_c is well above 1000 °C [25]. Ultimately, the synergy between this lowered T_c, which limits atomic diffusion, and the kinetic hindrance arising from severe lattice distortion prevents the complete reversal of the phase transition during cooling. Consequently, a portion of the high-temperature cubic phase is retained at room temperature in a metastable state, resulting in the formation of the dual-phase structure.

However, the microscopic spatial phase distribution corresponding to the composition-driven phase evolution (schematically illustrated in Fig. 2(a)) remains to be visualized. Conventional backscattered electron (BSE) imaging and energy dispersive X-ray spectroscopy (EDS) mapping (Figs. 2(b)–2(f)) were insufficient to distinguish the phases due to the identical chemical composition of the polymorphs. Consequently, EBSD was utilized to analyze the microstructure and phase distribution of representative samples (x = 0, 0.25, 0.5). As shown in Figs. S6(a)–S6(c) in the ESM, after Ar-ion polishing, the samples reveal their authentic microstructures. A considerable number of intergranular and intragranular pores are observed, which are likely attributed to Li volatilization at high temperatures [45,46]. Similar phenomena have been reported in previous studies [28,30,34].

The EBSD maps (Figs. 2(g)–2(i)) directly visualize the composition-driven phase evolution process, where the monoclinic ($C2/c$) and cubic ($Fm\bar{3}m$) phases are represented in blue and red, respectively. For LTO (Fig. 2(g)), the phase map consists exclusively of the monoclinic phase (blue regions), confirming its pure monoclinic structure. With the composition reaching $LTSN_{0.25}$ (Fig. 2(h)), the map clearly exhibits uniformly interwoven cubic and monoclinic phases, providing the most direct microscopic evidence for dual-phase coexistence. Interestingly, these two phases are not isolated in separate grains but coexist within individual grains [6]. Subsequently, upon increasing the composition to $LTSN_{0.5}$ (Fig. 2(i)), the phase map converts entirely to the cubic phase (red regions), verifying the thorough completion of the phase transition. Furthermore, to quantify the lattice distortion and strain induced by ionic substitution and the phase transition, the geometrically necessary dislocation (GND) density was analyzed. As illustrated in Fig. 2(j), LTO exhibits the lowest GND density with a homogeneous distribution, indicative of minimal lattice distortion. With the occurrence of the phase transition, the GND density in $LTSN_{0.25}$ (Fig. 2(k)) surges to its maximum level. This suggests that the lattice generates extensive GNDs to accommodate the severe local

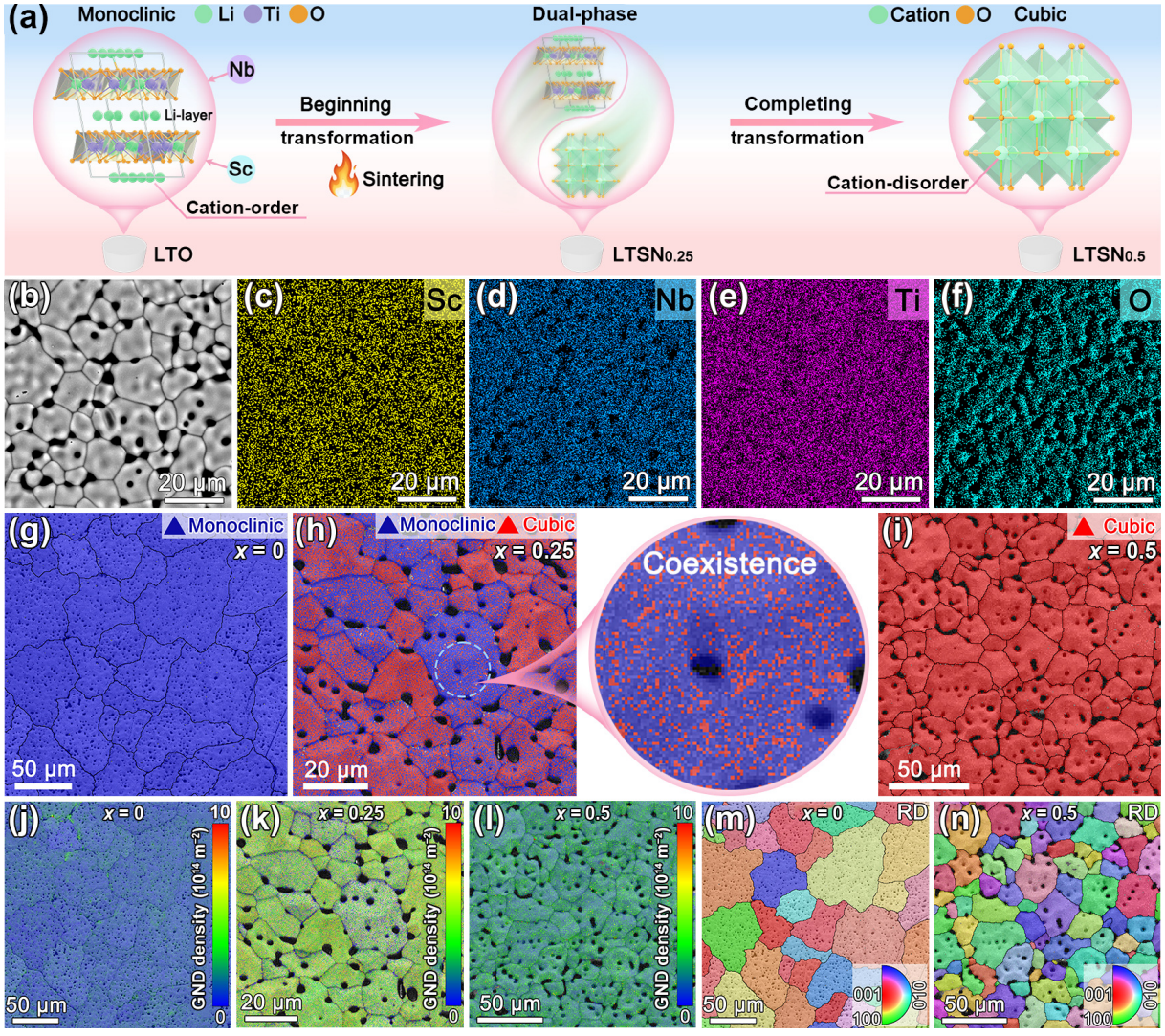

Fig. 2 EBSD analysis of microstructural evolution in $LTSN_x$ ceramics: (a) Schematic illustration of the structural evolution driven by compositional changes; (b) BSE image and (c–f) EDS elemental maps of the $LTSN_{0.25}$ ceramic; (g–i) EBSD phase maps and (j–l) GND density maps of $LTSN_x$ ceramics (x = 0, 0.25, 0.5); (m, n) grain orientation maps of $LTSN_x$ ceramics (x = 0, 0.5).

strain induced by the lattice mismatch between the coexisting phases [47,48]. For $LTSN_{0.5}$ (Fig. 2(l)), while the GND density is higher than that of LTO due to ionic substitution, it remains markedly lower than that of $LTSN_{0.25}$, pinpointing dual-phase lattice mismatch as the dominant source of local strain. Additionally, the random grain orientation observed in all samples (Figs. 2(m) and 2(n) and Fig. S6(d) in the ESM) rules out the existence of crystallographic texture.

To gain deeper insights into the crystal structural evolution and the cation order–disorder phase transition, atomic-scale characterization was performed on representative $LTSN_x$ (x = 0.1, 0.25, 0.4, 0.5) samples using SAED and HRTEM. Figure 3(b) presents the SAED pattern obtained from Region I of the $LTSN_{0.1}$ sample (corresponding to the area marked in Fig. 3(a)) along the [827] zone axis, which is highly consistent with the monoclinic structure. Notably, additional diffraction spots, identified as superlattice reflections (SRs), are observed between the fundamental reflections. These reflections typically signify the formation of an ordered superstructure resulting from the periodic modulation of the primitive rock-salt crystal structure. Similar phenomena have been reported in relevant LTO-based systems [11,26,28]. The HRTEM image taken along the [827] zone axis (Fig. 3(c)) clearly reveals lattice fringes matching the $(\bar{1}40)$ and $(2\bar{1}\bar{2})$ planes of the monoclinic phase. The corresponding crystal structure model is illustrated in Fig. 3(j). Furthermore, the fast Fourier transform (FFT) pattern (Fig. 3(d)) derived from Fig. 3(c) exhibits diffraction spots that reproduce the SAED pattern, further confirming the existence of the monoclinic superstructure.

Interestingly, the SAED pattern from region II of the $LTSN_{0.1}$ sample (Fig. 3(e)) exhibits a distinct difference from that of region I. The SAED pattern observed along the [001] zone axis (Fig. 3(f)), along with the corresponding HRTEM image (Fig. 3(g)) and its FFT (Fig. 3(h)), can be successfully indexed to the cubic rock-salt structure (with its atomic model depicted in Fig. 3(k)). This finding corroborates the dual-phase coexistence revealed by EBSD analysis. Compared to the simulated standard pattern for the cubic structure along the [001] zone axis (Fig. 3(i)), faint additional superlattice reflections are still observed between the fundamental reflections. These superlattice reflections align well with the cubic structure, and their Miller indices indicate a three-fold modulation of the primitive cubic periodicity [37]. Mechanistically, during the monoclinic-to-cubic phase transition, the formation of such superlattices introduces a higher degree of structural order, which reduces local entropy and consequently lowers dielectric loss [33]. Consistently, research by Bian *et al.* [14]

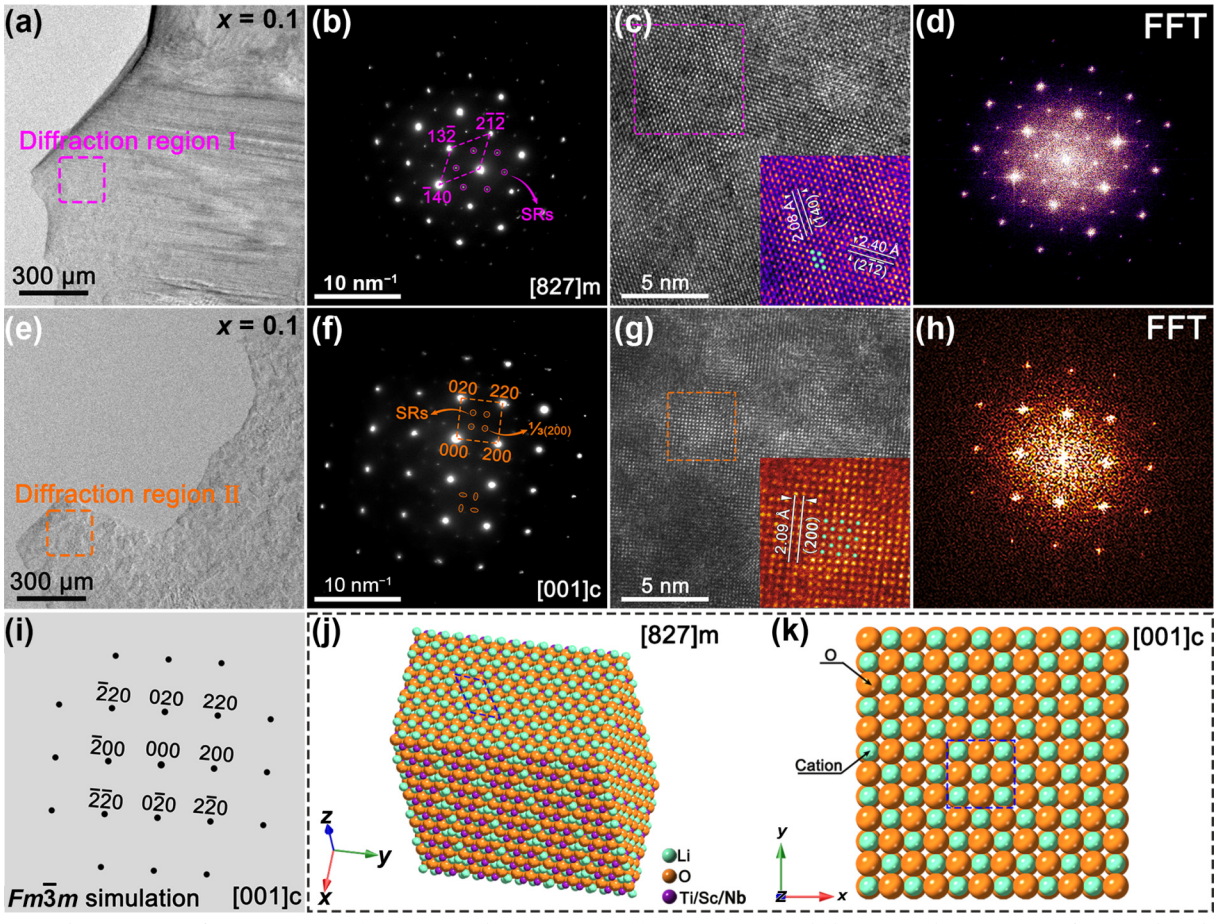

Fig. 3 TEM characterization of $LTSN_{0.1}$ ceramic: (a) TEM image, (b) SAED pattern, (c) HRTEM image, and (d) corresponding FFT image of region I along the [827] zone axis; (e) TEM image, (f) SAED pattern, (g) HRTEM image, and (h) corresponding FFT image of region II along the [001] zone axis; (i) simulated SAED pattern; (j, k) crystal structure models viewed along the corresponding zone axes.

on the Li_2TiO_3–MgO system demonstrates that the introduction of a low concentration of Mg^{2+} induces the formation of superlattices and ordered domains, thereby achieving ultra-high $Q\times f$ values. Similar phenomena have also been observed in systems such as $Ba(Zn_{1/3}Ta_{2/3})O_3$–$BaZrO_3$, $Li_2Ti_{1-x}(Cu_{1/3}Nb_{2/3})_xO_3$, and $Li_2Ti_{1-x}(Mg_{1/3}Nb_{2/3})_xO_3$ [11,28,49,50]. Collectively, these studies corroborate the strong correlation between the superstructure induced by aliovalent cation substitution and the low-loss properties of the material.

Notably, the intragranular dual-phase coexistence initially observed via EBSD is further corroborated by TEM analysis of the $LTSN_{0.25}$ sample. As illustrated in Fig. 4(b), the SAED pattern exhibits two distinct sets of diffraction spots within a single micro-region. Upon indexing, these reflections correspond to the cubic structure along the [1$\bar{1}$0] zone axis and the monoclinic structure along the [$\bar{1}$01] zone axis. The positions, interplanar angles, and *d*-spacings of all diffraction spots, as well as the FFT results (Figs. S7(b) and S7(d) in the ESM), match quantitatively with the simulated standard single-crystal diffraction patterns (Figs. S7(a) and S7(c) in the ESM). Furthermore, the HRTEM images (Figs. 4(c) and 4(d)) clearly resolve lattice fringe regions associated with both structures, displaying two significantly distinct lattice arrangements. To further corroborate the universality of this phenomenon, SAED and HRTEM results from another region of the $LTSN_{0.25}$ sample are provided in Figs. S7(e)–S7(h) in the ESM. This unique dual-phase microstructure plays a crucial role in regulating the microwave dielectric properties of $LTSN_x$ ceramics, particularly temperature stability. Furthermore, the elongated superlattice diffraction spots in Fig. S7(e) in the ESM indicate increased structural disorder, such as planar defects at high substitution levels, which tends to intensify phonon scattering and contribute to the degradation of the $Q\times f$ value.

As the substitution level x increases, SAED patterns observed along the [$\bar{1}$11] zone axis (Figs. 4(f) and 4(j)) clearly indicate that the $LTSN_x$ (x = 0.4, 0.5) ceramics have evolved into a stable, single-phase cubic structure. This experimental observation aligns perfectly with the simulated pattern (Fig. 4(h)). Additionally, the HRTEM images of the samples (x = 0.4 and 0.5) exhibit clear lattice fringes, where the identified interplanar spacings correspond to the (220) and ($\bar{2}$0$\bar{2}$) planes (Figs. 4(g) and 4(k)), further confirming the phase purity and the cubic symmetry. Moreover, no additional superlattice spots are observed in the SAED patterns for the x = 0.4 and 0.5 samples. The corresponding atomic model of the cubic structure is depicted in Fig. 4(l). Instead, hexagonal diffuse scattering appears around the fundamental diffraction spots (see hexagonal regions in Figs. 4(f) and 4(j)), indicating that the cation arrangement has tended toward disorder [26]. Furthermore, the highly uniform distribution of constituent elements (Fig. S8 in the ESM and Figs. 4(m1)–4(m4)) verifies the formation of the cubic solid solution. In summary, the microstructural transformation revealed by TEM is intrinsically correlated with the microwave dielectric properties of $LTSN_x$ ceramics, which will be discussed in detail below.

As illustrated in Fig. 5(a), within the continuous phase transition region ($0 \le x \le 0.4$), the TCF value exhibits a linear

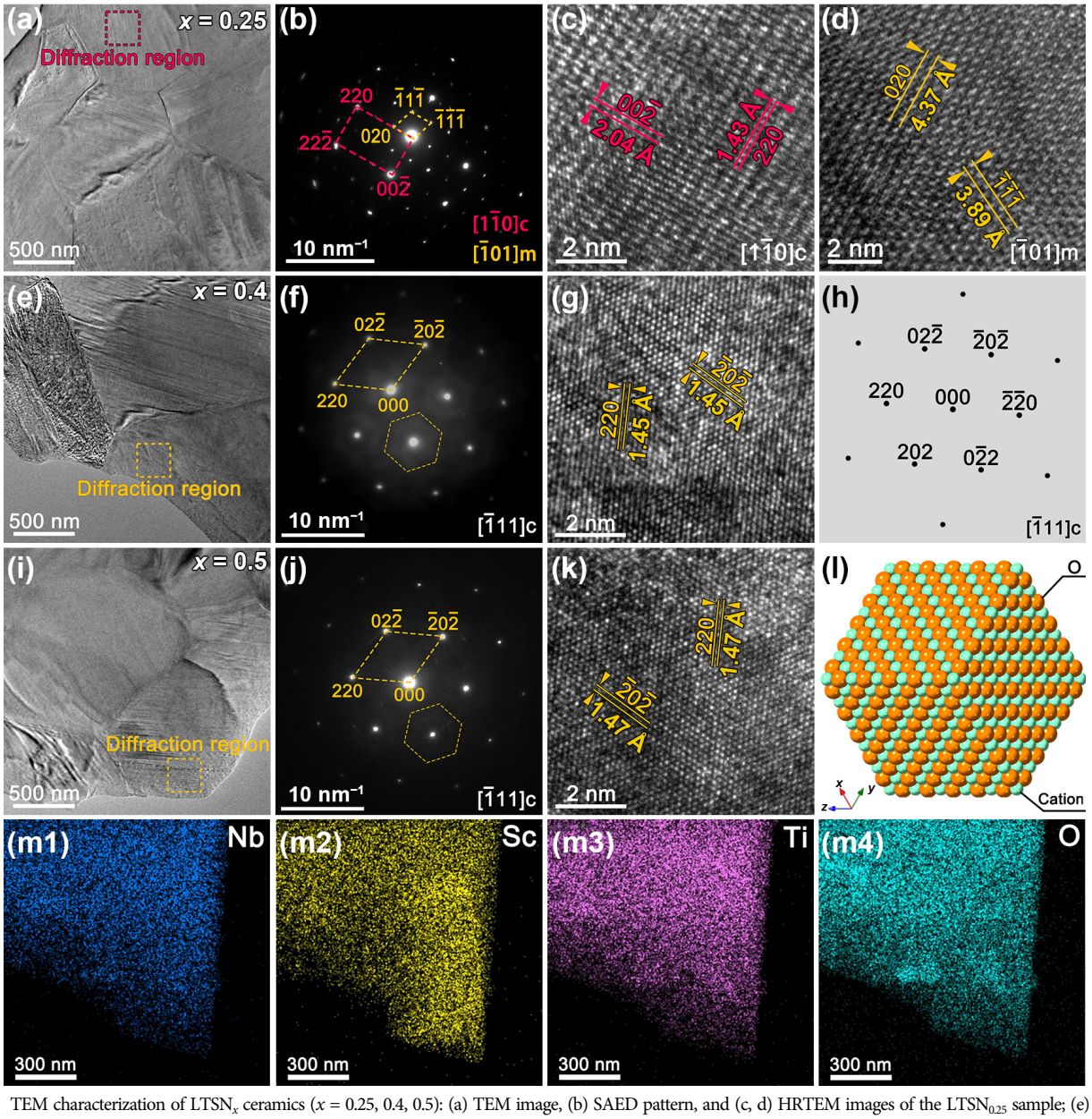

Fig. 4 TEM characterization of $LTSN_x$ ceramics (x = 0.25, 0.4, 0.5): (a) TEM image, (b) SAED pattern, and (c, d) HRTEM images of the $LTSN_{0.25}$ sample; (e) TEM image, (f) SAED pattern, and (g) HRTEM image of the $LTSN_{0.4}$ sample; (h) corresponding simulated SAED pattern; (i) TEM image, (j) SAED pattern, and (k) HRTEM image of the $LTSN_{0.5}$ sample; (l) cubic phase structure viewed along the [$\bar{1}$11] zone axis; (m1–m4) EDS elemental maps of the $LTSN_{0.5}$ sample.

decline from +34.3 to −22.2 ppm/°C, achieving a near-zero value of −2.3 ppm/°C at x = 0.25. Upon further increasing x to 0.5, the TCF plateaus at approximately −22 ppm/°C, confirming the completion of the phase transition. Given the dual-phase nature of this continuous solid solution series, the variation in TCF can be described by the Lichtenecker mixing rule (Eq. (2)) [51]:

$$\mathrm{TCF} = V_1\mathrm{TCF}_1 + V_2\mathrm{TCF}_2 \quad (2)$$

where TCF_1 and TCF_2 represent the TCF values of the two phases, and V_1 and V_2 are their corresponding volume fractions. In the region of low cubic phase content, the dominant monoclinic phase (positive TCF) maintains a positive overall TCF. As the cubic phase content increases, its negative TCF contribution intensifies, achieving a balance at x = 0.25 and ultimately causing the overall TCF to shift from positive to negative. The excellent agreement between the fitted values and the experimental results (Fig. S9 in the ESM) indicates that the dual-phase structure induced by $(Sc_{1/2}Nb_{1/2})^{4+}$ serves as the core mechanism for TCF tuning, effectively balancing the opposing TCF values of the two phases. Furthermore, the TCF of the material is collectively determined by the temperature coefficient of dielectric constant (τ_ε) and the linear thermal expansion coefficient (α_L), as expressed by Eq. (3) [21]:

$$\mathrm{TCF} = -\left(\frac{\tau_\varepsilon}{2} + \alpha\mathrm{L}\right) \quad (3)$$

As shown in Fig. 5(d), the α_L of the $LTSN_x$ ceramics (x = 0, 0.1, 0.25, 0.5) exhibits a marginal increase with rising x, which is attributed to the slightly higher intrinsic α_L of the cubic phase compared to that of the monoclinic phase. However, the overall increment in α_L amounts to only 1.25 ppm/°C, making its contribution to the TCF variation negligible. Further calculation based on the above equation yields τ_ε values of approximately −108.3 and +3.2 ppm/°C for the monoclinic and cubic phases, respectively, indicating that the TCF is primarily governed by τ_ε. This significant contrast likely stems from the distinct oxygen

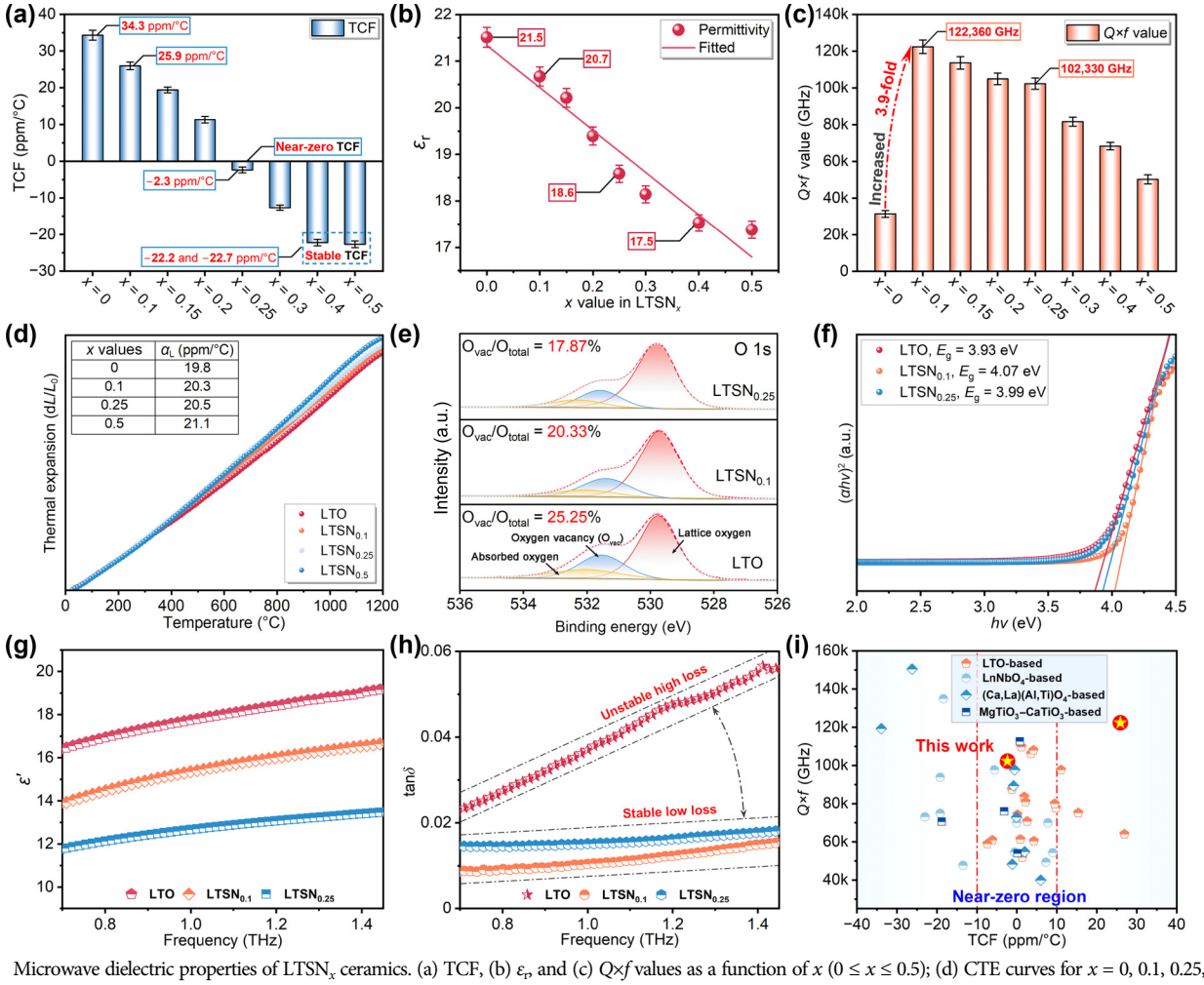

Fig. 5 Microwave dielectric properties of $LTSN_x$ ceramics. (a) TCF, (b) ε_r, and (c) $Q\times f$ values as a function of x ($0 \le x \le 0.5$); (d) CTE curves for x = 0, 0.1, 0.25, 0.5; (e) high-resolution O 1s XPS spectra and (f) fitted band gap values for x = 0, 0.1, 0.25; (g) ε' and (h) tanδ in the THz band (x = 0, 0.1, 0.25); (i) comparison of microwave dielectric properties between $LTSN_x$ ceramics and other representative K20 ceramics.

octahedral tilting behaviors, which fundamentally alter the temperature dependence of polarizability [14,52].

As illustrated in Fig. 5(b), the relative permittivity (ε_r) of $LTSN_x$ ceramics exhibits a linear decline with increasing x. Initially, the total molecular polarizability (defined as α_D ($LTSN_x$) = $2\alpha(Li^+)$ + $(1-x)\alpha(Ti^{4+})$ + $0.5x\alpha(Sc^{3+})$ + $0.5x\alpha(Nb^{5+})$ + $3\alpha(O^{2-})$) shows an increasing trend with x (Fig. S10(a) in the ESM), primarily due to the higher effective ionic polarizability of the $(Sc_{1/2}Nb_{1/2})^{4+}$ cluster (3.39 Å^3) than that of Ti^{4+} (2.93 Å^3) [53]. However, according to the Clausius–Mossotti equation, the macroscopic dielectric response is fundamentally governed by the polarizability per unit volume (α/V_m). As shown in Fig. S10(b) in the ESM, the lattice expansion outweighs the increase in molecular polarizability, ultimately causing an overall downward trend in the calculated α/V_m. This downward trend perfectly aligns with the decline of the measured ε_r. Moreover, ε_r is also closely related to the variation in phase fraction. Notably, the pure cubic $LTSN_{0.4}$ and $LTSN_{0.5}$ exhibit comparably low ε_r values similar to most cubic rock-salt materials (Fig. S11 in the ESM), which can be attributed to their high structural symmetry restricting ionic displacement [54]. The ε_r of the dual-phase solid solutions follows the Lichtenecker empirical rule (Eq. (4)) [55]:

$$\ln\varepsilon_r = V_1\ln\varepsilon_{r1} + V_2\ln\varepsilon_{r2} \quad (4)$$

where V_1, ε_{r1} and V_2, ε_{r2} represent the volume fractions and dielectric constants of the two constituent phases, respectively. With increasing cubic phase content, the calculated and measured values exhibit a highly consistent downward trend (Fig. S12 in the ESM), indicating that ε_r is simultaneously influenced by the evolution of phase composition.

For microwave devices, high Q is critical for achieving superior frequency selectivity and ultra-low insertion loss. As illustrated in Fig. 5(c), the substitution of $(Sc_{1/2}Nb_{1/2})^{4+}$ for Ti^{4+} yields a remarkable enhancement in the $Q\times f$ values of LTO ceramics. Specifically, the $Q\times f$ value peaks at ~ 122,360 GHz for x = 0.1, representing a nearly 3.9-fold increase over that of pure LTO (31,430 GHz). Despite the monotonic decline observed across the range of $0.1 \le x \le 0.5$, the sample at x = 0.25 retains an ultra-high $Q\times f$ value of ~102,330 GHz. The variation in $Q\times f$ is governed by a complex interplay of factors, including microstructure, lattice defects, and the cation order–disorder transition [33]. As depicted in Figs. S13(a)–S13(h) in the ESM, the $LTSN_x$ ceramics exhibit a porous morphology, a typical feature of Li-rich materials originating from Li volatilization during high-temperature sintering [12,56]. Of particular interest is the presence of microcracks in both LTO and $LTSN_{0.1}$ samples, which likely originate from the cleavage of weak Li–O bonds along the (002) plane, induced by lattice stress during the cation order–disorder phase transition [14,56]. Generally, the presence of such pores and microcracks inevitably exacerbates extrinsic loss (Eq. (S1) in the ESM), which is inconsistent with the ultra-low loss performance achieved in the $LTSN_{0.1}$ sample. Meanwhile, within the range of $0.3 \le x \le 0.5$, a significant increase in the average grain size is

observed (Fig. S14 in the ESM), which may be attributed to the intensified phase transition. Generally, a larger grain size typically reduces grain boundary scattering and lowers extrinsic loss, which contradicts the observed decreasing trend of the $Q\times f$ value in this range. Furthermore, all $LTSN_x$ ceramics display a consistently porous internal microstructure with no discernible differences among samples (Figs. S15(a)–S15(h) in the ESM), further indicating that the microstructural morphology exerts a limited influence on dielectric loss.

During high-temperature sintering under low oxygen partial pressure, Ti^{4+} ions in Ti-based ceramics are prone to reduction to Ti^{3+} [57,58]. This reduction, coupled with the simultaneous volatilization of Li, facilitates the formation of oxygen vacancies. To probe the chemical states and defect evolution, XPS analysis was performed, with binding energies calibrated against the C 1s peak (284.8 eV). The survey and high-resolution spectra (Figs. S16(a), S16(c), and S16(d) in the ESM) clearly identify the characteristic peaks of Nb 3d and Sc 2p, verifying the presence of Nb^{5+} and Sc^{3+} [7,31]. The high stability of these valence states effectively circumvents the dielectric loss associated with d–d electron transitions. To further quantify the defect concentration, the high-resolution O 1s spectra were analyzed (Fig. 5(e)). Three deconvoluted peaks are identified, corresponding to lattice oxygen (529.7 eV), oxygen vacancies (531.6 eV, O_{vac}), and absorbed oxygen (532.5 eV) [59,60]. Upon the introduction of $(Sc_{1/2}Nb_{1/2})^{4+}$, the relative proportion of oxygen vacancies (calculated as the area ratio of O_{vac} to the total peak area) decreases notably from 25.25% in LTO to 20.33% and 17.87% for the x = 0.1 and x = 0.25 samples, respectively. Concurrently, a corresponding reduction in the Ti^{3+} concentration is observed (Fig. S16(b) in the ESM). These results demonstrate that $(Sc_{1/2}Nb_{1/2})^{4+}$ substitution effectively suppresses the reduction of Ti^{4+} and the formation of oxygen vacancies, thereby mitigating the dielectric loss induced by such defects and contributing significantly to the enhanced $Q\times f$ values [33,61]. Correspondingly, the band gap energy (E_g) widens to 4.07 eV for $LTSN_{0.1}$ and 3.99 eV for $LTSN_{0.25}$, both surpassing that of pure LTO (3.93 eV, Fig. 5(f)). The lower E_g of $LTSN_{0.25}$ compared to $LTSN_{0.1}$ is possibly due to excessive $(Sc_{1/2}Nb_{1/2})^{4+}$ doping, causing overlapping impurity bands and band tails, which reduce E_g [57]. This enhancement may be attributed to the reduction of defect energy levels resulting from the suppressed formation of oxygen vacancies, as well as the incorporation of wide-bandgap oxides [62]. A wider E_g signifies a higher energy barrier for electron excitation from the valence band to the conduction band, which is conducive to reducing conduction loss [57,61].

Furthermore, the variation in dielectric loss is intrinsically linked to the structural evolution. In analogous rock-salt systems such as $Li_2Ti_{1-x}(Mg_{1/3}Nb_{2/3})_xO_3$, $Li_2Ti_{1-x}(Al_{1/2}Nb_{1/2})_xO_3$, and $Li_3Mg_{2-x/3}Sn_xNb_{1-2x/3}O_6$, a substantial enhancement in $Q\times f$ values is commonly observed during the initial stage of the phase transition [11,34,37]. In this work, the reconstructed superlattices observed at x = 0.1 imply that minor aliovalent substitution of Ti^{4+} by $(Sc_{1/2}Nb_{1/2})^{4+}$ complex ions drives this unique structural ordering. Such structural reconstruction facilitates the reduction of anharmonic lattice vibrations and the suppression of intrinsic dielectric loss, analogous to the mechanism in perovskite ceramics [63,64]. Overall, the realization of ultra-high $Q\times f$ values in $LTSN_x$ ceramics results from the synergistic interaction between substitution-induced reconstructed superlattices and the suppression of structural defects. Subsequently, within the range of $0.1 \le x \le 0.5$, the linear decline in $Q\times f$ values is attributed to the increasing cubic phase content, which intensifies long-range disorder and consequently escalates dielectric loss [30].

Consequently, driven by the phase transition effect, the $LTSN_{0.25}$ ceramic exhibits ultra-low dielectric loss ($Q\times f$ = 102,330 GHz), excellent temperature stability (TCF = −2.3 ppm/°C), and a lower bulk density (3.02 g/cm^3, Fig. S18 in the ESM). This material surpasses most currently reported K20 systems (Fig. 5(i) and Tables S1 and S2 in the ESM) in terms of microwave dielectric properties and shows high potential for the design of next-generation lightweight ceramics.

As communication technologies evolve from 5.5G toward the 6G era, THz communication is increasingly recognized as a critical technology. Therefore, evaluating the dielectric response in the terahertz frequency band is essential. Figures 5(g) and 5(h) and Figs. S19(a)–S19(c) in the ESM present the optical and dielectric properties of $LTSN_x$ (x = 0, 0.1, 0.25) ceramics in the 0.7–1.45 THz range. The refractive index (n), absorption coefficient (α), and real permittivity (ε') all increase with frequency, a trend consistent with previous reports [29,37,65]. Notably, the ε' values are significantly lower than those measured in the microwave region ($TE_{01\delta}$ mode, Fig. 5(g)), which is likely related to the relaxation of defect-induced slow polarizations at high frequencies [66]. The substitution of Ti^{4+} by $(Sc_{1/2}Nb_{1/2})^{4+}$ optimizes the defect concentration, thereby regulating these slow polarizations and leading to the significantly lower ε' observed in the THz range. ε' decreases with increasing x, consistent with the trend observed in the microwave region. In contrast to LTO, $LTSN_{0.1}$ and $LTSN_{0.25}$ show lower and more stable dielectric losses (Fig. 5(h)), suggesting excellent suitability for THz applications, benefiting from the suppressed anharmonic lattice vibrations and reduced lattice defects, as discussed above.

To evaluate the application potential of $LTSN_{0.25}$ ceramic for the n79 band, two distinct filter structures—a monoblock (type-1) and a dual-layer (type-2)—were designed and simulated (Fig. 6(a)). For the simulation, ε_r and tanδ of the $LTSN_{0.25}$ model were set to 18.6 and 7.58×10^{-5} (corresponding to Q = 13,180), respectively. As presented in Fig. 6(b), the type-1 filter exhibits excellent impedance matching (S_{11} < −20 dB; minimum −53.8 dB) across a wide passband of 4.7–5.0 GHz (bandwidth ≈ 300 MHz). Crucially, an ultra-low insertion loss (S_{21}) of 0.40 dB is consistently maintained across this operating bandwidth, directly attributed to the intrinsic high Q of the material. The dual-layer design type-2) demonstrated similarly robust performance (Fig. 6(c)). Even with a compact stacked architecture, the device maintains an ultra-low insertion loss of 0.30 dB. Furthermore, this design displays steep rejection skirts with stopband attenuation exceeding 50 dB at 4.4 and 5.4 GHz. Notably, two transmission zeros were achieved near the passband for both structures, significantly enhancing the selectivity of the filters [67]. These results collectively confirm that the $LTSN_{0.25}$ ceramic maintain exceptional signal integrity across varying device architectures, validating its potential for next-generation, high-performance RF components. Thermal analysis and infrared thermographic results of the $LTSN_{0.25}$ ceramic are provided in Figs. S20–S26 in the ESM.

4 Conclusions

In summary, a novel dual-phase structural regulation strategy is demonstrated to address the critical performance bottlenecks of LTO-based microwave dielectric ceramics. Structural analyses reveal that $(Sc_{1/2}Nb_{1/2})^{4+}$ substitution drives a continuous monoclinic-to-cubic phase transition with increasing doping levels. Crucially, the stabilization of the high-temperature cubic phase is attributed to the combined effects of the reduction in T_c and the induced lattice distortion. The variation in the relative content of the monoclinic and cubic phases effectively modulates

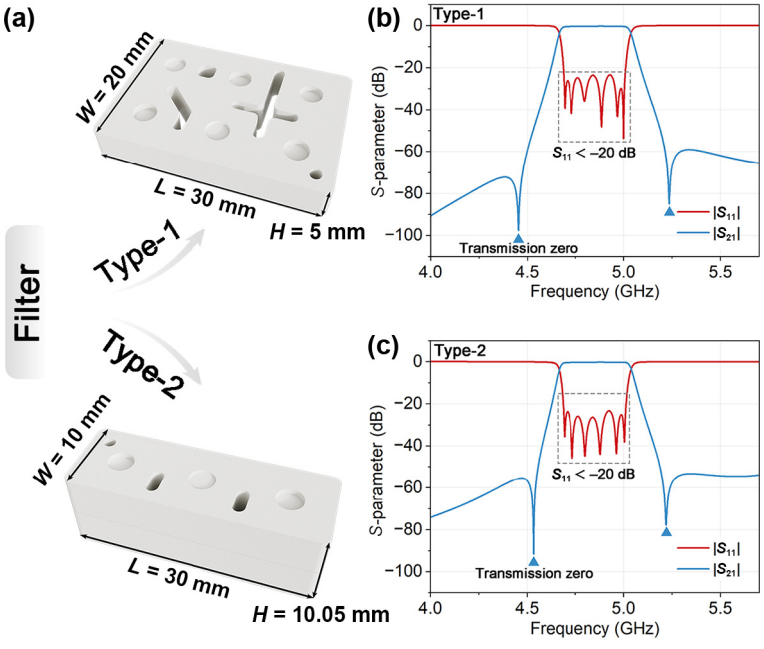

Fig. 6 (a) Simulated 3D models and (b, c) simulated *S*-parameters of the type-1 and type-2 filters.

the microwave dielectric properties, particularly the dielectric constant and TCF. Meanwhile, the achievement of ultra-high $Q\times f$ is ascribed to the local superlattice reconstruction and the inhibition of lattice defects, which significantly suppress extrinsic dielectric loss. Consequently, superior microwave dielectric performance is achieved in the $LTSN_{0.25}$ ceramic, including an ε_r of 18.6, a remarkable $Q\times f$ value of 102,330 GHz (at 7.76 GHz), and a near-zero TCF of −2.3 ppm/°C. Additionally, the practical potential of the $LTSN_{0.25}$ ceramic for 5.5G applications is comprehensively validated by its terahertz dielectric response, thermal management capability, and simulated filter performance. This work opens new avenues for designing high-performance microwave dielectric ceramics for next-generation wireless communication systems.

Acknowledgements

This work was supported by the Jiangxi Provincial Natural Science Foundation (Nos. 20252BAC240019 and 20224BAB214020), Jingdezhen Municipal Science and Technology Program (No. 2025JCYJ001), and Opening Project of National Engineering Research Center for Domestic & Building Ceramics (No. GXZX2303).

Availability of data and materials

The data are available from the corresponding author upon reasonable request.

Competing interests

The authors have no competing interests to declare that are relevant to the content of this article. The author Zong-Yang Shen is the Associate Editor of this journal.

Electronic Supplementary Material

Supplementary material is available in the online version of this article at https://doi.org/10.26599/JAC.2026.9221305.

References

[1] Yang K, He CG, Fang JM, *et al.* Advanced RF filters for wireless communications. *Chip* 2023, **2**: 100058.

[2] Yao Y, Wang YY, Bafrooei HB, *et al.* Ni–Co complex ionic synergistically modifying octahedron lattice of cordierite ceramics for the application of 5G microwave–millimeter-wave antennas. *Inorg Chem* 2024, **63**: 10022–10030.

[3] Liu H, Liu Y, Yu XQ, *et al.* A high-performance, temperature-stable $Mg_{1.99}Ga_{0.01}Si_{0.99}Al_{0.01}O_4$–$CaTiO_3$ microwave dielectric ceramic and its 5G/6G waveguide filter. *J Eur Ceram Soc* 2023, **43**: 7471–7477.

[4] Xu YQ, Larsson EG, Jorswieck EA, *et al.* Distributed signal processing for extremely large-scale antenna array systems: State-of-the-art and future directions. *IEEE J Sel Top Signa* 2025, **19**: 304–330.

[5] Shehbaz M, Du C, Zhou D, *et al.* Recent progress in dielectric resonator antenna: Materials, designs, fabrications, and their performance. *Appl Phys Rev* 2023, **10**: 021303.

[6] Wang ZW, Guo HH, Huang YY, *et al.* Synergistic dual-phase and microstructure engineering toward temperature-stable, ultra-low loss Li_2TiO_3-based microwave dielectric ceramic. *Adv Funct Mater* 2026, **36**: e18002.

[7] Wu FF, Sun RX, Du C, *et al.* P^{5+}-enhanced novel samarium niobate ultralow-loss microwave ceramics as dielectric resonator for X-band antenna applications. *Adv Funct Mater* 2025, **35**: 2421225.

[8] Xu XY, Zhou X, Wu HT, *et al.* Bonding characteristics, electrical and microwave/terahertz dielectric properties of novel tetragonal scheelite structure $NaSrLnMo_3O_{12}$ (Ln = Ce, Pr, Eu, Y, Yb) ceramics for antenna application. *J Adv Ceram* 2025, **14**: 9221179.

[9] Kulsartov TV, Gordienko YN, Tazhibayeva IL, *et al.* Tritium migration in the materials proposed for fusion reactors: Li_2TiO_3 and beryllium. *J Nucl Mater* 2013, **442**: S740–S745.

[10] Islam MM, Bredow T. Lithium diffusion pathways in β-Li_2TiO_3: A theoretical study. *J Phys Chem C* 2016, **120**: 7061–7066.

[11] Guo HH, Zhou D, Pang LX, *et al.* Influence of $(Mg_{1/3}Nb_{2/3})$ complex substitutions on crystal structures and microwave dielectric properties of Li_2TiO_3 ceramics with extreme low loss. *J Materiomics* 2018, **4**: 368–382.

[12] Pang LX, Zhou D. Microwave dielectric properties of low-firing Li_2MO_3 (M = Ti, Zr, Sn) ceramics with B_2O_3–CuO addition. *J Am Ceram Soc* 2010, **93**: 3614–3617.

[13] Guo HH, Zhou D, Du C, *et al.* Temperature stable $Li_2Ti_{0.75}(Mg_{1/3}Nb_{2/3})_{0.25}O_3$-based microwave dielectric ceramics with low sintering temperature and ultra-low dielectric loss for dielectric resonator antenna applications. *J Mater Chem C* 2020, **8**: 4690–4700.

[14] Bian JJ, Dong YF. New high Q microwave dielectric ceramics with

rock salt structures: $(1-x)Li_2TiO_3+xMgO$ system ($0 \le x \le 0.5$). *J Eur Ceram Soc* 2010, **30**: 325–330.
[15] Lai YM, Hong CY, Jin LC, *et al.* Temperature stability and high-Qf of low temperature firing Mg_2SiO_4–Li_2TiO_3 microwave dielectric ceramics. *Ceram Int* 2017, **43**: 16167–16173.
[16] Liu XL, Wang ZX, She XY, *et al.* Improved microstructure and high quality factor of $Li_2Ti_{0.9}(Zn_{1/3}Ta_{2/3})_{0.1}O_3$ microwave ceramics with LiF additive for LTCC applications. *J Eur Ceram Soc* 2023, **43**: 1469–1476.
[17] Liu WQ, Zuo RZ. A novel Li_2TiO_3–Li_2CeO_3 ceramic composite with excellent microwave dielectric properties for low-temperature cofired ceramic applications. *J Eur Ceram Soc* 2018, **38**: 119–123.
[18] Sayyadi-Shahraki A, Taheri-Nassaj E, Hassanzadeh-Tabrizi SA, *et al.* A new temperature stable microwave dielectric ceramic with low-sintering temperature in Li_2TiO_3–$Li_2Zn_3Ti_4O_{12}$ system. *J Alloy Compd* 2014, **597**: 161–166.
[19] Zhou D, Zhang L, Xu DM, *et al.* Novel method to achieve temperature-stable microwave dielectric ceramics: A case in the fergusonite-structured $NdNbO_4$ system. *ACS Appl Mater Inter* 2023, **15**: 19129–19136.
[20] Park HS, Yoon KH, Kim ES. Relationship between the bond valence and the temperature coefficient of the resonant frequency in the complex perovskite $(Pb_{1-x}Ca_x)[Fe_{0.5}(Nb_{1-y}Ta_y)_{0.5}]O_3$. *J Am Ceram Soc* 2001, **84**: 99–103.
[21] Guo HH, Zhou D, Liu WF, *et al.* Microwave dielectric properties of temperature-stable zircon-type $(Bi,Ce)VO_4$ solid solution ceramics. *J Am Ceram Soc* 2020, **103**: 423–431.
[22] Xiang HC, Zhang YH, Chen JQ, *et al.* Structure evolution and τ_f influence mechanism of $Bi_{1-x}Ho_xVO_4$ microwave dielectric ceramics for LTCC applications. *J Mater Sci Technol* 2024, **197**: 1–8.
[23] Zhou D, Pang LX, Guo J, *et al.* Influence of Ce substitution for Bi in $BiVO_4$ and the impact on the phase evolution and microwave dielectric properties. *Inorg Chem* 2014, **53**: 1048–1055.
[24] Wu FF, Zhou D, Du C, *et al.* Design and fabrication of a satellite communication dielectric resonator antenna with novel low loss and temperature-stabilized $(Sm_{1-x}Ca_x)(Nb_{1-x}Mo_x)O_4$ (x = 0.15–0.7) microwave ceramics. *Chem Mater* 2023, **35**: 104–115.
[25] Castellanos M, West AR. Order–disorder phenomena in oxides with rock salt structures: The system Li_2TiO_3–Mg0. *J Mater Sci* 1979, **14**: 450–454.
[26] Leu LC, Bian JJ, Gout D, *et al.* Order–disorder transition in the $(1-x)Li_2TiO_3$–xMgO system ($0 \le x \le 0.5$). *RSC Adv* 2012, **2**: 1598–1604.
[27] Mather GC, Dussarrat C, Etourneau J, *et al.* A review of cation-ordered rock salt superstructure oxides. *J Mater Chem* 2000, **10**: 2219–2230.
[28] Guo HH, Fu MS, Zhou D, *et al.* Design of a high-efficiency and -gain antenna using novel low-loss, temperature-stable $Li_2Ti_{1-x}(Cu_{1/3}Nb_{2/3})_xO_3$ microwave dielectric ceramics. *ACS Appl Mater Inter* 2021, **13**: 912–923.
[29] Liu LT, Guo WJ, Yan SJ, *et al.* Microstructure, Raman spectroscopy, THz time domain spectrum and microwave dielectric properties of $Li_2Ti_{1-x}(Zn_{1/3}Ta_{2/3})_xO_3$ ceramics. *Ceram Int* 2023, **49**: 6864–6872.
[30] Bian JJ, Zhang XH. Structural evolution, grain growth kinetics and microwave dielectric properties of $Li_2Ti_{1-x}(Mg_{1/3}Nb_{2/3})_xO_3$. *J Eur Ceram Soc* 2018, **38**: 599–604.
[31] Li WY, Xian Y, Deng HN, *et al.* Sc^{3+}-modified Mg–Al–Mn–Fe–O spinel ceramics with co-enhanced microwave dielectric and thermosensitive properties for multifunctional applications. *J Adv Ceram* 2025, **14**: 9221153.
[32] Moriya K, Kumakura S, Kim EJ, *et al.* Electrode performance of P′ 2-$Na_{2/3}[Mn_{1-x}Sc_x]O_2$ in sodium batteries. *Electrochem Commun* 2025, **174**: 107891.
[33] Reaney IM, Iddles D. Microwave dielectric ceramics for resonators and filters in mobile phone networks. *J Am Ceram Soc* 2006, **89**: 2063–2072.
[34] Zhang TW, Zuo RZ, Zhang J. Structure, microwave dielectric properties, and low-temperature sintering of acceptor/donor codoped $Li_2Ti_{1-x}(Al_{0.5}Nb_{0.5})_xO_3$ ceramics. *J Am Ceram Soc* 2016, **99**: 825–832.
[35] Yang YK, Liu FL, Zhang YW, *et al.* Microwave dielectric properties of ultra-low loss $Li_2MgTi_{0.7}(Mg_{1/3}Nb_{2/3})_{0.3}O_4$ ceramics sintered at low temperature by LiF addition. *Ceram Int* 2018, **44**: 12238–12244.
[36] Yuan LL, Bian JJ. Microwave dielectric properties of the lithium containing compounds with rock salt structure. *Ferroelectrics* 2009, **387**: 123–129.
[37] Zhang X, Fang ZX, Yang HY, *et al.* Lattice evolution, ordering transformation and microwave dielectric properties of rock-salt $Li_{3+x}Mg_{2-2x}Nb_{1-x}Ti_{2x}O_6$ solid-solution system: A newly developed pseudo ternary phase diagram. *Acta Mater* 2021, **206**: 116636.
[38] Kroumova E, Aroyo MI, Perez-Mato JM, *et al.* Bilbao crystallographic server: Useful databases and tools for phase-transition studies. *Phase Transit* 2003, **76**: 155–170.
[39] Clarke DR, Adar F. Measurement of the crystallographically transformed zone produced by fracture in ceramics containing tetragonal zirconia. *J Am Ceram Soc* 1982, **65**: 284–288.
[40] Pelletier MJ. Quantitative analysis using Raman spectrometry. *Appl Spectrosc* 2003, **57**: 20A–42A.
[41] Chen LC, Berenson R, Birman JL. Space-group selection rules: "Rocksalt" O_h^5–$Fm3m$. *Phys Rev* 1968, **170**: 639–648.
[42] Ishikawa K, Fujima N, Komura H. First-order Raman scattering in MgO microcrystals. *J Appl Phys* 1985, **57**: 973–975.
[43] Shrivastava A, Desai V, Chaudhuri P. Thermal expansion studies of Li_2TiO_3 by dilatometry and *in-situ* high-temperature X-ray diffraction. *Ceram Int* 2024, **50**: 1756–1763.
[44] Wen KC, Lv WQ, He WD. Interfacial lattice-strain effects on improving the overall performance of micro-solid oxide fuel cells. *J Mater Chem A* 2015, **3**: 20031–20050.
[45] Bian JJ, Dong YF. Sintering behavior, microstructure and microwave dielectric properties of $Li_{2+x}TiO_3$ ($0 \le x \le 0.2$). *Mater Sci Eng B-Adv* 2011, **176**: 147–151.
[46] Gierszewski P. Review of properties of lithium metatitanate. *Fusion Eng Des* 1998, **39**: 739–743.
[47] Zhao C, Li X. Quantitative study of residual strain and geometrically necessary dislocation density using HR-EBSD method. *Exp Mech* 2021, **61**: 1281–1290.
[48] Shimokawa T, Fujii K, Niiyama T. Atomic simulation study of the factors affecting nucleation in deformation-induced martensitic transformation in grains and at grain boundaries in pure iron. *Acta Mater* 2024, **265**: 119629.
[49] Davies PK, Tong JZ, Negas T. Effect of ordering-induced domain boundaries on low-loss $Ba(Zn_{1/3}Ta_{2/3})O_3$–$BaZrO_3$ perovskite microwave dielectrics. *J Am Ceram Soc* 1997, **80**: 1727–1740.
[50] Chai L, Davies PK. Formation and structural characterization of 1:1 ordered perovskites in the $Ba(Zn_{1/3}Ta_{2/3})O_3$–$BaZrO_3$ system. *J Am Ceram Soc* 1997, **80**: 3193–3198.
[51] Chu X, Gan L, Jiang J, *et al.* The doping-induced phase transition in rock salt-structured $Li_2Ti_{1-x}(Mg_{1/3}Ta_{2/3})_xO_3$ ($0 \le x \le 0.4$) ceramics revealed by EBSD and XRD refinement and its effects on the microwave dielectric properties. *Mater Today Commun* 2023, **37**: 107145.
[52] Lai YM, Tang XL, Huang X, *et al.* Phase composition, crystal structure and microwave dielectric properties of $Mg_{2-x}Cu_xSiO_4$ ceramics. *J Eur Ceram Soc* 2018, **38**: 1508–1516.
[53] Shannon RD. Dielectric polarizabilities of ions in oxides and fluorides. *J Appl Phys* 1993, **73**: 348–366.
[54] Luo WJ, Li LX, Yu SH, *et al.* Effects of structural characteristics on microwave dielectric properties of low-loss $(Zn_{1-x}Ni_x)ZrNbTaO_8$ ceramics. *Ceram Int* 2018, **44**: 12414–12419.
[55] Yin CZ, Tang Y, Chen JQ, *et al.* Two low-permittivity melilite ceramics in the SrO–MO–GeO_2 (M = Mg, Zn) system and their temperature stability through compositional modifications. *J Eur Ceram Soc* 2020, **40**: 1186–1190.

[56] Huang CL, Tseng YW, Chen JY. High-*Q* dielectrics using ZnO-modified Li_2TiO_3 ceramics for microwave applications. *J Eur Ceram Soc* 2012, **32**: 3287–3295.
[57] Ma LZ, Jiang LX, Duan JH, *et al.* Enhanced microwave performance in spinel dielectric ceramics using entropy strategy for 5G/6G communication devices. *Chem Eng J* 2025, **503**: 158159.
[58] Huang YY, Wang ZW, Guo HH, *et al.* Manipulating microwave dielectric properties of Li_2TiO_3-based ceramics through chemical doping-controlled phase modulation engineering. *Ceram Int* 2025, **51**: 58809–58816.
[59] Ullah B, Lei W, Wang XH, *et al.* Dielectric and ferroelectric behavior of an incipient ferroelectric $Sr_{(1-3x/2)}Ce_xTiO_3$ novel solid solution. *RSC Adv* 2016, **6**: 91679–91688.
[60] Xie MJ, Lai YM, Xiang PW, *et al.* The entropy effect on the structure and microwave dielectric properties of high-entropy $Li_x(MgZnCoNi)_{(1-x)/4}Al_2O_{4-\delta}$ ceramics. *Chem Eng J* 2024, **496**: 154132.
[61] Ma LZ, Duan JH, Jiang LX, *et al.* High-entropy enhanced microwave dielectric performance. *Compos Part B—Eng* 2025, **303**: 112545.
[62] Zeng FF, Zhang QS, Zhang SD, *et al.* Enhanced energy-storage performances and thermal stability in BNT–LST-based ceramics by tuning domain configuration and bandgap. *Rare Metals* 2025, **44**: 3313–3323.
[63] Matsumoto H, Tamura H, Wakino K. $Ba(Mg,Ta)O_3$–$BaSnO_3$ high-*Q* dielectric resonator. *Jpn J Appl Phys* 1991, **30**: 2347.
[64] Tamura H, Konoike T, Sakabe Y, *et al.* Improved high-*Q* dielectric resonator with complex perovskite structure. *J Am Ceram Soc* 1984, **67**: 59–61.
[65] Lu YT, Guo WJ, Zhang CY, *et al.* Microwave/terahertz dielectric properties of high-*Q* willemite ceramics: Dual control through non-stoichiometric design and Ge^{4+} substitution. *J Materiomics* 2026, **12**: 101118.
[66] Lu Y, Zhang Q, Wu Q, *et al.* Giant enhancement of THz-frequency optical nonlinearity by phonon polariton in ionic crystals. *Nat Commun* 2021, **12**: 3183.
[67] Liu H, Cao L, Gu JC, *et al.* High-entropy processed high quality and low-temperature cofired $LiMgPO_4$-based dielectric ceramics for low-loss packaged millimeter-wave filters. *J Eur Ceram Soc* 2025, **45**: 116957.